# S. Deogekar

Department of Mechanical, Aerospace and Nuclear Engineering, Rensselaer Polytechnic Institute, Troy, NY 12180 e-mail: deoges@rpi.edu

### Z. Yan

Department of Mechanical, Aerospace and Nuclear Engineering, Rensselaer Polytechnic Institute, Troy, NY 12180 e-mail: yanz6@rpi.edu

### R. C. Picu

Department of Mechanical, Aerospace and Nuclear Engineering, Rensselaer Polytechnic Institute, Troy, NY 12180 e-mail: picuc@rpi.edu

# **Random Fiber Networks With Superior Properties Through Network Topology Control**

In this work, we study the effect of network architecture on the nonlinear elastic behavior and strength of athermal random fiber networks of cellular type. We introduce a topology modification of Poisson-Voronoi (PV) networks with convex cells, leading to networks with stochastic nonconvex cells. Geometric measures are developed to characterize this new class of nonconvex Voronoi (NCV) networks. These are softer than the reference PV networks at the same nominal network parameters such as density, cross-link density, fiber diameter, and connectivity number. Their response is linear elastic over a broad range of strains, unlike PV networks that exhibit a gradual increase of the tangent stiffness starting from small strains. NCV networks exhibit much smaller Poisson contraction than any network of same nominal parameters. Interestingly, the strength of NCV networks increases continuously with an increasing degree of nonconvexity of the cells. These exceptional properties render this class of networks of interest in a variety of applications, such as tissue scaffolds, nonwovens, and protective clothing. [DOI: 10.1115/1.4043828]

#### 1 Introduction

Materials made from, or containing, fibers are a common occurrence in our everyday lives. A subset of these are "network materials," in which the fibers are connected in a random network that percolates through the domain occupied by the respective object. In network materials, the fiber network performs the central structural function and, in most cases, determines the mechanical properties of the material.

Examples of network materials include nonwovens, paper and cellulose products, insulation, buckypaper, rubber, and gels [1–3]. Biological materials are mostly of network type. Collagen and elastin fibers are the essential components of connective tissue. various membranes, and blood vessels in the animal and human bodies and define the mechanical properties of these biological entities [4–6].

The relationship between the network structure and mechanics has been a subject of intense research over the last several decades [7–14]. In networks with limited internal dissipation (e.g., due to viscoelastic fibers or interfiber friction) and which do not accumulate damage during loading, the response is hyperelastic. This response is characterized by three regimes [15,16]: a linear elastic response is observed at small strains (regime I), followed by the power law or exponential stiffening (regime II), after which the response becomes linear again at larger strains and stresses (regime III). Two parameters are typically used to characterize this behavior: the small strain modulus  $E_0$ , which is representative for regime I, and the type of strain hardening taking place in regime II. Strain hardening can be either of exponential or powerlaw type and depends on network architecture [17].

Damage occurs in networks either by fiber or cross-link rupture. Failure of cross-links is more common, as observed in paper [18– 20] and nonwovens [21–24] and is likely the dominating failure mechanism in most biological networks. Damage initiation may begin in any of the three regimes described here, the function of the strength of the cross-links (or/and fibers). Damage accumulation reflects at the macroscale as a gradual reduction of the tangent stiffness. Networks being stochastic by definition, damage accumulation,

localization, and failure are complex processes tightly coupled with the network architecture. The relation between network strength and material parameters was discussed in a number of publications [19,25-31].

Defining the relationship between structure and properties is a long-standing quest in materials science. In random networks, this effort is rendered more complex by the difficulty of defining what is meant by "structure." Here, we divide the quantities used to define the network structure in three categories: (a) parameters controlled when the network is constructed, (b) geometric parameters measurable in the network, but which are not directly controllable, and (c) aspects of the network architecture. Typical parameters of type (a) are the density  $\rho$  (total length of fiber per unit volume) and material properties of fibers. For elastic fibers, the characteristic fiber properties are their axial and bending rigidities  $E_fA$  and  $E_fI$ , where  $E_f$  represents the modulus of the fiber material and A and I are the area and moment of inertia of the fiber cross section. Note that the two rigidities are not independent if the fiber cross section is circular, since  $A \sim d^2$  and  $I \sim d^4$ , where d is the fiber diameter. However, situations exist when A and I are independent parameters, as for example with molecular bundles (silk, tropocollagen). The cross-link number density (total number of cross-links per unit volume)  $\rho_b$  may be a parameter of type (a) or (b) in different applications. The connectivity index  $\bar{z}$  representing the mean number of segments emerging from a cross-link is a parameter of type (a). Preferential fiber orientation is characterized by the orientation tensor, which is typically measured after the network is constructed, and hence is a parameter of type (b). In most works, random networks are characterized exclusively using these five parameters:  $\rho$ ,  $\rho_b$ ,  $\bar{z}$ ,  $E_f A$ , and  $E_f I$ .

It was established [32] that, when  $\rho$ ,  $\rho_b$ , and/or  $E_I$  are small, the small strain network modulus scales as  $E_0 \sim \rho^x E_f I$  (where exponent x depends on the network architecture and network embedding space dimensionality), while in the opposite situation  $E_0 \sim \rho E_f A$ . This indicates that, in the first case, fibers deform predominantly in their bending mode and network deformation is nonaffine, while in the second case, fibers deform predominantly in their axial mode, which implies that network deformation is approximately affine. This general behavior is independent of the network architecture, but the transition from one type of scaling to the other happens at different values of the respective parameters in networks of different architectures.

Parameters of type (c) are more difficult to define. It may be observed that, in general, random networks are of two types: cellular

<sup>&</sup>lt;sup>1</sup>Corresponding author.

Contributed by the Applied Mechanics Division of ASME for publication in the JOURNAL OF APPLIED MECHANICS. Manuscript received March 18, 2019; final manuscript received May 2, 2019; published online June 4, 2019. Assoc. Editor: Thomas

and fibrous. Cellular networks resemble open cell foams and are composed of fibers with two cross-links per fiber, located at the two fiber ends. Fibrous networks are composed of long fibers, which are not necessarily straight, each having multiple cross-links with other fibers. Most biological networks, as well as nonwovens, paper, cellulose products, and insulation, are of a fibrous type.

The mechanical behavior of random fibrous and cellular networks is qualitatively the same, but with some important differences. For example, the exponent x of the power law dependence of  $E_0$  on  $\rho$  is x=2 for cellular networks (same as for open cell foams [33–35]), and x=3 for fibrous networks (see experimental and numerical results in Refs. [17,36,37]). Furthermore, cellular networks strain stiffen exponentially, while fibrous networks exhibit a power law strain stiffening relation [17].

Progress in relating the mechanics of cellular networks to elements of the network architecture has been made beyond these general considerations, as discussed in the literature on open cell foams [38–43]. The parameter used to characterize the architecture, in this case, is the polydispersity of cell volumes. If the density is kept constant, increasing cell volume polydispersity leads to a reduction of the modulus and of the yield stress (when the foam material is elastic-plastic) or of the onset of shear localization (when the foam material is elastic) [38,41]. This is similar to the behavior of stochastic composites in which the material subdomains have elastic constants selected from a distribution. As the variance of the distribution of local properties increases while the mean is kept constant, the homogenized elastic constants of the composite decrease [44,45]. If the fluctuating local parameter is the yield stress, the homogenized yield stress also decreases with increasing variability [46].

Fibrous networks have a more disordered microstructure than cellular networks and identifying parameters that describe the architecture beyond the five structural parameters of types (a) and (b) specified above is difficult.

In this work, we focus on cellular networks and explore the effect on the mechanical behavior of a new parameter of type (c) characterizing the cell shape. We keep all structural parameters of types (a) and (b), as well as the polydispersity of cell sizes constant, and explore the effect of introducing variability in the shape of the cells, allowing some of the cells to become nonconvex. It is shown that this has a significant effect on mechanical properties. This defines a class of networks, which we name nonconvex Voronoi (NCV) networks, with unusual properties, which we expect may be important in various applications.

# 2 Geometric Considerations: Definition of Nonconvex Voronoi Network Architecture

In this section, we establish NCV as a class of stochastic cellular networks and contrast this architecture with that of Voronoi cellular networks with controlled cell volume variability.

In order to isolate the effect of the cell shape variability characteristic for NCV on the mechanical behavior of the network, we aim to work with networks in which all other parameters of types (a) and (b) are constant. The connectivity parameter in cellular networks in 3D is  $\bar{z} = 4$ . We aim to generate a family of networks, starting from a periodic network with no randomness, and control independently the cell size and cell shape variability.

Since we wish to construct networks of the same connectivity at all cross-links, we consider the Archimedean solids, which are polyhedra composed of regular polygons that meet at identical vertices. Not all 13 Archimedean solids are space filling. Therefore, we look for the intersection of the set of Archimedean solids with the set of plesiohedra (space-filling polyhedra) with exactly four edges meeting at each vertex z = 4. This intersection contains two types of cells: the truncated octahedron and the truncated icosahedron.

A different perspective on this issue is obtained when starting with the class of parallelohedra, which are polyhedra that fill space such that each cell can be obtained from another cell by translation without rotation. There are five parallelohedra: the cube, which, when forming a network has z = 6, the hexagonal prism,

with z=5, the elongated dodecahedron, with z=5, the rhombic dodecahedron which has two types of vertices, and hence,  $\bar{z}$  of the resulting network is between 4 and 5, and the truncated octahedron, with z=4.

Therefore, we select as the reference periodic network with no disorder, a honeycomb of truncated octahedra, known also with the more generic name of tetrakaidecahedra. This type of structure was considered in most works on open cell foams (e.g., Refs. [39,42,43]). Such a network can be obtained by Voronoi tessellating a body-centered cubic (BCC) lattice of points (seeds).

Randomness can be introduced in this structure in two ways, as defined by the following two network generation procedures:

Procedure 1: The starting point of this procedure is the periodic truncated octahedral honeycomb (TOH), Fig. 1(a), which results by Voronoi tessellating a periodic BCC lattice of seed points. Random displacements are given to the position of these seeds. Increasing the magnitude of these displacements leads, after tessellation, to increasingly irregular cells. The connectivity parameter remains z = 4, but the number of faces per cell and the number of edges per face vary from cell to cell and the variability becomes more pronounced as the magnitude of the seed displacements increase [47]. This procedure was used to construct the family of open cell foams studied in Refs. [39,42,43]. Since the Voronoi tessellation is used to produce networks from all these spatial arrangements of seeds, the cells are always convex. The limit structure (corresponding to maximum disorder) obtained through this procedure is that which would otherwise result by Voronoi tessellating a random spatial distribution of seeds. This is denoted as the Poisson-Voronoi (PV) network (as the seeds are obtained from a Poisson process, Fig. 1(b)). The transition of the network structure from TOH to PV was studied in Ref. [47].

Procedure 2: The starting point of this procedure is the PV network. This network is perturbed by applying random displacements (of magnitude  $\delta$ ) to the cross-links. This does not affect the connectivity of the network, which remains z=4, and does not change the distribution of the number of faces per cell and the number of edges per face. Likewise, the cross-link density  $\rho_b$  remains unchanged as perturbation is introduced, while the density  $\rho$  increases as  $\delta$  increases. As discussed below, the cells become gradually nonconvex as  $\delta$  increases. The average cell volume is independent of  $\delta$ . This procedure is used to generate NCV networks (Fig. 1(c)).

Comparing the two procedures, it results that procedure 1 produces networks of convex cells of increasing cell volume variability [47], while procedure 2 produces networks with increasing cell nonconvexity, without modifying the statistics of other parameters describing fiber connectivity and cell structure. Here, we focus on the class of NCV networks produced using procedure 2.

Since the parameter  $\delta$  describing the degree of perturbation applied to the PV networks is only of algorithmic importance, it is useful to develop a related parameter that can be controlled or measured in experiments. To this end, we start with the observation that the density of the network  $\rho$  is related to the mean segment length  $l_c$  through the 3D equivalent of the Kallmes–Corte relation for 2D Mikado networks [31,48]:

$$\rho l_c^2 = q \tag{1}$$

where q is an architecture-specific constant. In the current work, fibers are straight between cross-links. If the crimp is present, relation (1) is still valid, with q becoming a function of crimp [31].

Figure 2(a) shows the variation of  $\rho$  with  $l_c$  for the TOH regular network, for PV networks, and for a family of NCV networks with increasing  $\delta$ . All edges of the truncated octahedron are of the same length  $l_c$ , the total volume of the polyhedron is  $8\sqrt{2}l_o^2$ , and the total length of fiber per unit volume is  $\rho = (3\sqrt{2}/4)l_c^{-2}$ . Therefore, for the regular TOH network  $q = 3\sqrt{2}/4 = 1.06$ . The value of q for the PV network is obtained numerically and results q = 0.95 (Fig. 2(a)). It is seen that TOH and PV networks, i.e., the two limit types of networks produced using procedure 1, have values of q, which are very close to each other. However, q increases

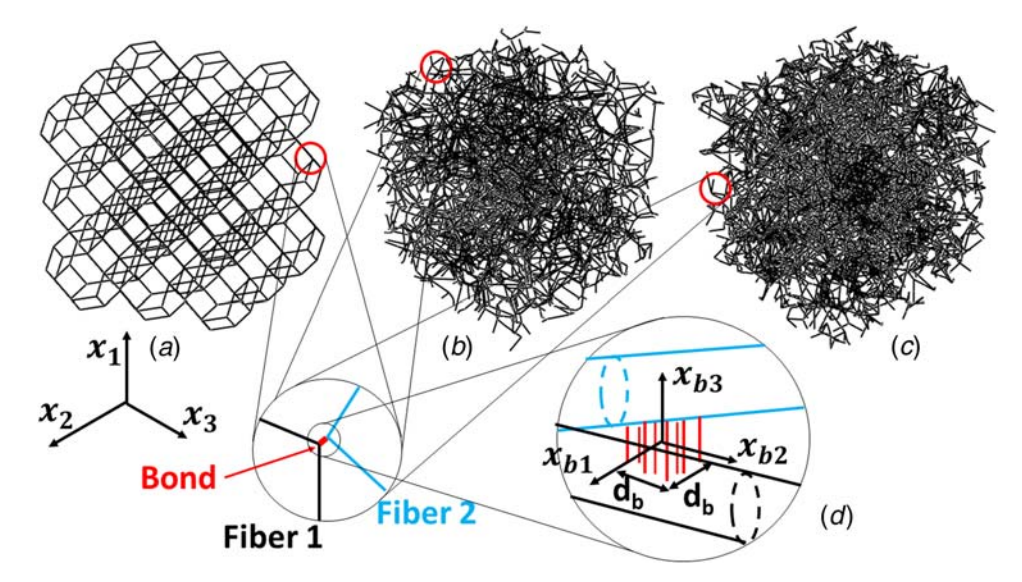
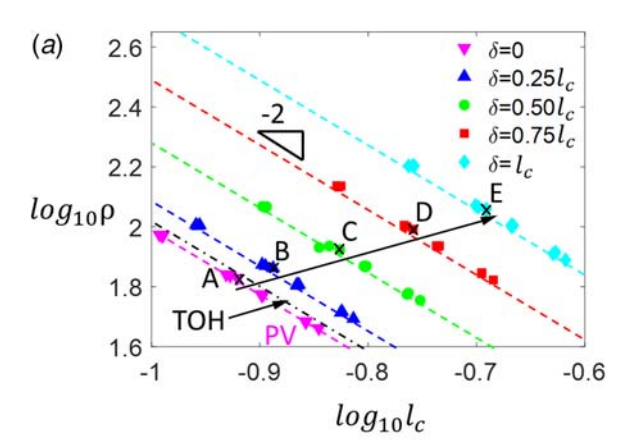


Fig. 1 Realizations of the (a) periodic truncated octahedral honeycomb (TOH) network, (b) Poisson–Voronoi (PV) network, and (c) nonconvex Voronoi (NCV) network



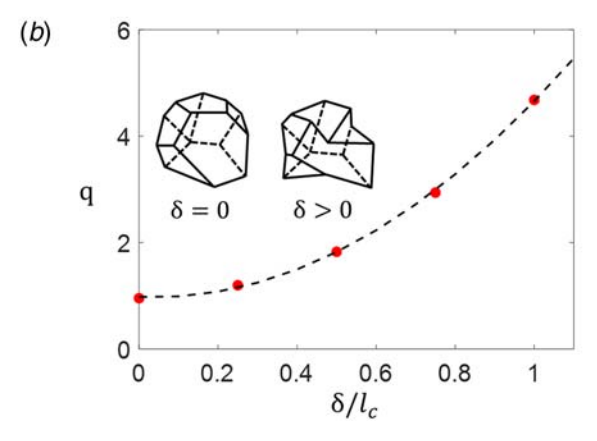


Fig. 2 (a) Modified Kallmes–Corte-type relation for the 3D networks considered in this study and (b) dependence of parameter q on the perturbation  $\delta$ . The inset shows representative convex and nonconvex cells.

monotonically with  $\delta$  for NCV networks produced using procedure 2. Therefore, q is a parameter that discriminates between these two classes of structures and is descriptive for NCV networks. Figure 2(b) shows the variation of q with  $\delta$ .

We note that using q is also desirable because it can be evaluated in experiments based on  $\rho$  and  $l_c$ ,  $\rho$  is a parameter of type (a) and is controlled when the network is constructed or can be easily

measured a posteriori, while  $l_c$  can be measured by direct observation of the network.

To characterize the size and shape of the cells obtained with the two network generation procedures and further relate parameters  $\delta$  and q to the resulting architectures, we evaluate the volumes of the cells and a measure of their nonconvexity. For convex cells, the cell volume  $V_i$  results directly from the Voronoi tessellation procedure. To evaluate the volume of a nonconvex cell, we use the procedure outlined in the Appendix. For each network, the mean and coefficient of variation of the distribution of cell volumes are evaluated. To quantify the cell nonconvexity, we use the relative difference between the volume of the convex hull of the vertices of a given cell  $V_i^{ch}$  and the actual volume of the cell  $V_i$  computed with the procedure described in the Appendix. This quantity is normalized by  $V_i^{PV}$ , the volume of the corresponding cell in the PV network (prior to undergoing procedure 2), to get the nonconvexity parameter  $\beta_i$  for the cell.

$$\beta_i = \frac{|V_i^{ch} - V_i|}{V_i^{PV}} \tag{2}$$

The network-scale nonconvexity parameter  $\bar{\beta}$  is computed as the average of  $\beta_i$  over all cells i of the given network. The variability of cell volumes is quantified using the coefficient of variation  $\sigma_V/\bar{V}$  of the  $V_i$  distribution.

Figure 3(a) shows the coefficient of variation of the cell volumes  $\sigma_V/\bar{V}$  as a function of the perturbation for networks produced by the two procedures. Figure 3(b) shows the variation of the nonconvexity parameter  $\bar{\beta}$  with the perturbation. In each of the two figures, the left panel refers to networks produced by procedure 1. In this case, the perturbation is applied to the seeds of the Voronoi tessellation and is represented here as  $\delta^*$  normalized by the mean segment length of the TOH network with no perturbation  $l_c$ . The resulting networks range from TOH to PV. These have convex cells and hence  $\beta = 0$ , while the cell volumes are increasingly polydisperse as the perturbation  $\delta^*$  increases. The right panel corresponds to NCV networks generated by procedure 2. In this case, the perturbation refers to the parameter  $\delta$  used in Fig. 2 and related to q of Eq. (2) as shown in Fig. 2(b).  $\delta$  is normalized by the mean segment length of the PV network. We observe that in NCV networks, the cell volume variability is independent of the perturbation, while the cells become progressively more nonconvex as  $\delta$  (or q) increases. This quantifies the difference between Voronoi networks of polydisperse convex cells (from TOH to PV) and the NCV networks of nonconvex cells.

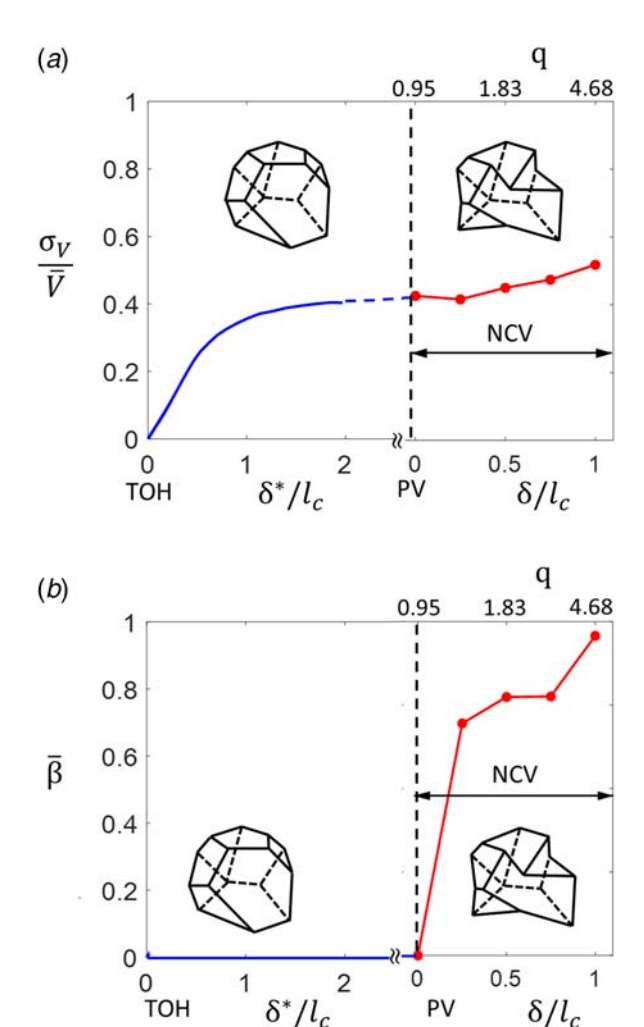
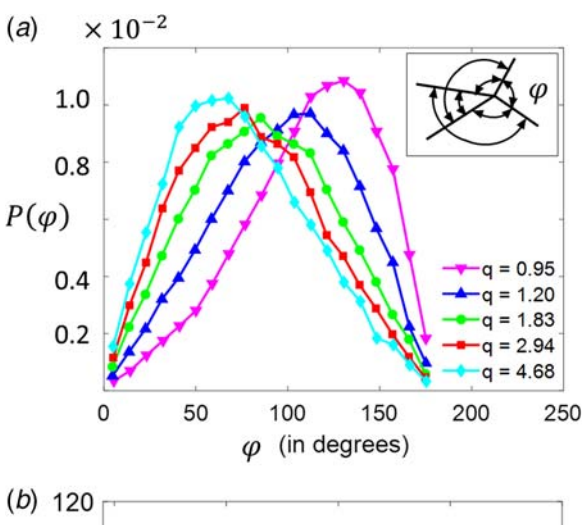


Fig. 3 (a) Coefficient of variation of cell volumes  $\sigma_V/\bar{V}$  and (b) measure of cell nonconvexity  $\bar{\beta}$  versus perturbation. In each figure, the left panel refers to the perturbation of seeds of the Voronoi tessellation leading, through procedure 1, to the gradual transition from the periodic TOH structure to the PV random structures. The right panel refers to NCV networks obtained, through procedure 2, by perturbing the nodes of a PV with increasing random displacements  $\delta$ . The data indicate that NCV networks have nonconvex cells ( $\bar{\beta} > 0$ ), while cell volume polydispersity does not increase with  $\delta$ . The curve in the left panel of (a) is based on the data from Ref. [47]. The inset figures show representative convex and nonconvex cells.

In order to relate the structural parameters  $\delta$  and q to other geometric measures of NCV networks that can be obtained by direct observations of physical networks, we present in Fig. 4(a), the distribution of fiber-to-fiber angles at cross-links  $\varphi$  for NCV networks with several q values. As the degree of structural disorder increases, the distribution of  $\varphi$  shifts to the left, indicating that fibers make more acute angles. The variation of the mean of the distribution  $\bar{\varphi}$  with q is shown in Fig. 4(b). This provides an alternative way to evaluate q based on direct observations of physical networks and hence  $\sigma_V/\bar{V}$  and  $\bar{\beta}$  from Fig. 3.

A discussion of the methods that can be used to manufacture such networks is required. Various additive manufacturing (AM) methods have been used recently to construct periodic and random cellular materials [49–51]. The selection of the AM method depends on the desired fiber material. Selective laser sintering is commonly used in case of ceramic [52] or polymeric fibers [53], while selective laser melting [54] or electron beam melting [55] are used for metallic fibers. Another popular choice due to its simplicity is 3D printing [56] and this method has been used for printing patient-specific



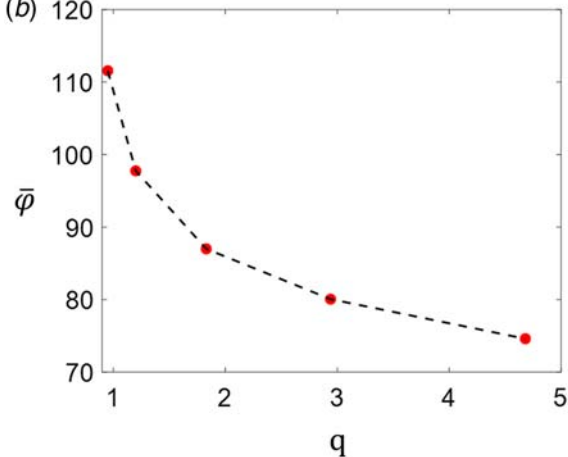


Fig. 4 (a) Distributions of interfiber angles at crosslinks  $\varphi$  for NCV networks of various degrees of disorder quantified by the parameter q. The inset shows the six pairs of interfiber angles  $\varphi$  measured at each cross-link. (b) Variation of the mean of the distributions in (a)  $\bar{\varphi}$  with q.

replacement tissues. A review of the influence of different AM methods on the geometrical features and mechanical properties of cellular materials can be found in Ref. [51].

### 3 Models and Methods

The procedure used to construct NCV networks is described above: seed points are distributed randomly in a cubic domain. These are used to construct a PV tessellation and the edges of the resulting polyhedra are considered fibers, while the vertices are considered cross-links. Further, the cross-link positions are modified by random displacements of magnitude  $\delta$ . Values of  $\delta$  ranging from 0 to  $l_c$  are considered, where  $l_c$  is the mean segment length of the PV network.

Fibers are straight between any two cross-links and have a circular cross section of diameter d. When working with networks composed of fibers of the same type, parameter  $l_b = \sqrt{E_f I/E_f A}$  proves convenient [7,10]. For fibers with circular section,  $l_b = d/4$ . We consider  $l_b$  values from 0.001 to 0.01. The excluded volume interaction between fibers, i.e., the formation of contacts at sites other than the cross-links, is not considered in these models. Excluded volume contributions to mechanics are weak under tensile loading due to the large free volume of the network [17].

The interfiber cross-links are represented as connectors with axial and bending stiffness and are allowed to rupture at a prescribed effective load. The failure of networks is generally associated with cross-link rupture (e.g., in bonded nonwovens and paper) [19,21,57].

The connector stiffness is approximately two orders of magnitude larger than the axial and bending stiffness of a fiber segment of length equal to the mean segment length  $l_c$ . This ensures that the maximum cross-link deformation is always smaller than  $6 \times 10^{-3} d$ , such that cross-link deformation does not contribute to the overall network kinematics. This is the situation in most athermal networks. Cases in which cross-links are formed by proteins that may undergo large deformations before failure also exist in biomolecular networks [58,59], but these are outside the scope of the present discussion.

Cross-link failure is modeled as described in the previous publications [25,31]. To summarize, the force and moments associated with the deformation of the cross-link are defined in the coordinate system of the cross-link  $\{x_{b1}, x_{b2}, x_{b3}\}$  shown in Fig. 1(d), as  $F_{bi} = K_{bF}u_{bi}$  and  $M_{bi} = K_{bM}\theta_{bi}$ , where  $u_{bi}$  and  $\theta_{bi}$  are the ith components of the relative displacement and relative rotation of the two fibers in contact, respectively, and  $K_{bF}$  and  $K_{bM}$  are the effective bond stiffnesses in the translational and rotational modes, respectively. The bond failure criterion is written as

$$F_{eq} = \sqrt{F_{b1}^2 + F_{b2}^2 + F_{b3} - \frac{6}{d_b} \sqrt{M_{b1}^2 + M_{b2}^2}} = f_c$$
 (3)

where  $F_{b1}$ ,  $F_{b2}$ , and  $F_{b3}$  are the forces transmitted by the bond in the direction of the three local coordinate axes, and  $M_{b1}$  and  $M_{b2}$  are the moments transmitted by the bond about the local axes  $x_{b1}$  and  $x_{b2}$ .  $d_b$  represents the characteristic size of the bond  $(d_b < d)$ .  $\langle \cdot \rangle$  indicates Macaulay bracket, which vanishes if the quantity in the bracket is negative and is equal to the respective quantity when it is positive.  $f_c$  represents the critical equivalent force that causes bond failure and is considered a material parameter.

Fibers are discretized using multiple Timoshenko beam elements such to ensure adequate representation of the beam kinematics, while retaining computational efficiency. The cross-links are modeled as uncoupled springs with both translational and rotational stiffness (using the connector element CONN3D2 and the connector section BUSHING in ABAQUS).

The model is loaded in uniaxial tension by imposing displacements to the nodes on opposite faces of the model in the direction of the loading. The other degrees of freedom of the respective nodes are left free. Lateral surfaces of the model are constrained to remain planar but are free to move in the direction perpendicular to the loading direction, to ensure zero average tractions.

The solution is obtained using the general purpose finite element solver ABAQUS/EXPLICIT Version 6.13-1. The dynamic scheme used introduces inertial effects. These are negligible before the onset of cross-link failure, but become important at larger strains. A numerical damping scheme (bulk viscosity) is used in order to minimize the contribution of inertial forces. The kinetic energy is limited to 1% of the total energy prior to the onset of cross-link failure and to 5% of the total energy up to a strain larger than that corresponding to the peak stress. All sections of the stress-strain curves shown here with symbols and continuous line correspond to conditions in which this restriction is fulfilled. In addition, we compute the second Piola-Kirchoff (PK2) stress by taking the derivative of the strain energy density relative to the Green-Lagrange strain and then compute the Cauchy stress from the PK2 stress. This procedure further limits the inertia effects, as discussed in Appendix A of Ref. [25]. The values of the Cauchy stress reported here are obtained using this procedure. This method leads to stress values comparable to those obtained from a much more expensive simulation performed with a strain rate one-order of magnitude smaller and with larger algorithmic damping, which can be considered quasi-static.

# 4 Mechanical Behavior of Nonconvex Voronoi Networks

**4.1 Small Strain Stiffness.** As discussed in Sec. 1, the small strain stiffness  $E_0$  is a function of  $\rho$  and fiber properties. This is best represented in a plot such as that shown in Fig. 5(a), which

establishes the relation between network stiffness and structural parameters of types (a) and (b). The plot shows  $E_0$ , normalized by  $\rho E_f A$ , versus the nondimensional group  $\rho I_b^2$ . The affine model prediction for the modulus is  $E_0^{aff} = \alpha \rho E_f A$ , where  $\alpha$  is a numerical constant equal to  $\sim 0.1$ . This value is the upper limit of the modulus of all realizations of the network with given  $\rho$  and is independent of the network architecture.

The plot in Fig. 5(a) has two regimes. At large  $\rho l_b^2$ ,  $E_0$  asymptotes toward  $E_0^{aff}$ . In such conditions, the network deforms almost affinely and stores energy predominantly in the axial deformation mode of fibers (hence, the proportionality of  $E_0$  with  $E_fA$ ). At small  $\rho l_b^2$ , the network deforms nonaffinely and  $E_0 \sim \rho^2 E_f I$ . The quadratic scaling of the modulus with the density is common to all cellular networks and to open cell foams [33]. The proportionality of  $E_0$  with  $E_f I$  indicates that the main deformation mode of fibers is bending.

Data for networks of increasing q are shown along with the curve corresponding to the reference PV model. The shape of the curve does not depend on q and  $E_0 \sim \rho^2$  in the nonaffine regime for all NCV networks considered. The dependence of the stiffness on fiber properties is identical to that of the PV case  $(E_0 \sim E_f A)$  in the affine regime and  $E_0 \sim E_f I$  in the nonaffine regime). This is expected since the basic fiber-level mechanics is independent of q. However, the curves shift gradually to lower values of the ordinate as q increases.

Perturbing the network by  $\delta$  increases the mean segment length  $l_c$ , which leads to fiber segments of larger slenderness ratio  $d/l_c$ , which are more prone to bending. To demonstrate this argument, we use Eq. (1) and the definition of  $l_b$  for fibers with circular section ( $l_b = d/4$ ) to rewrite the nondimensional group on the horizontal axis in Fig. 5(a) as  $\rho l_b^2 \sim (d/l_c)^2$ . Note that  $d/l_c$  is the

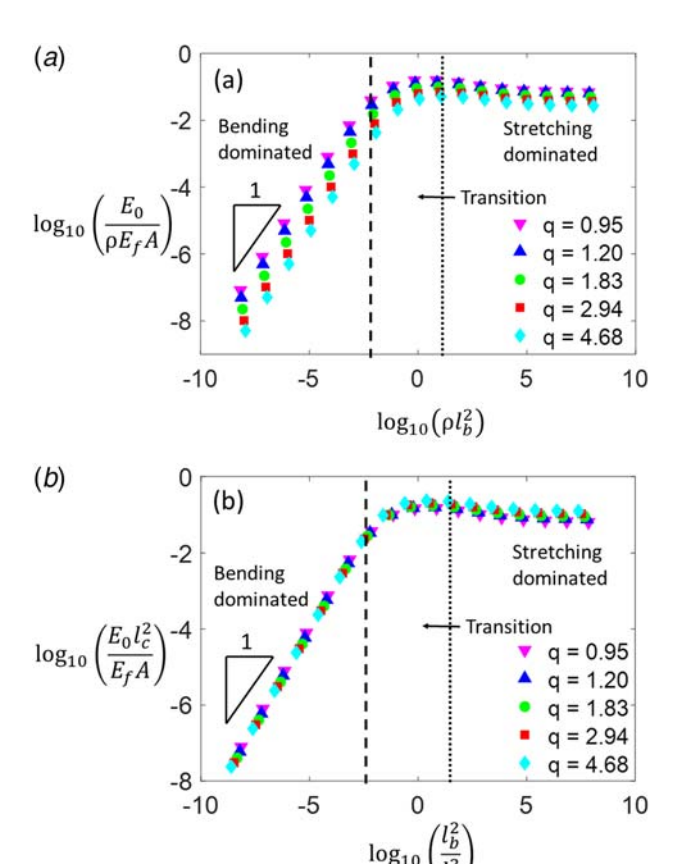


Fig. 5 (a) Relation between the small strain stiffness of the network and structural parameters for various NCV networks with increasing degree of nonconvexity and (b) data in (a) replotted in terms of the mean fiber length  $I_{\rm c}$  showing full data collapse

aspect ratio of the average fiber segment. The data in Fig. 5(a) are replotted in Fig. 5(b) after  $\rho$  in the normalization factor of  $E_0$  is also written in terms of  $l_c$  using Eq. (1). This leads to the collapse of all curves, which indicates that the mean segment length  $l_c$ , instead of network density  $\rho$ , is the controlling parameter in this case.

**4.2 Large Deformations.** Significantly more pronounced differences between PV and NCV networks are observed when the large deformation behavior is analyzed. Consider first a set of NCV networks that are obtained from the same PV network by gradually increasing  $\delta$  (or q). This set corresponds to a locus in Fig. 2(a), which is a straight line that intersects the lines of constant q as shown. The configurations selected for the present discussion are indicated by A, B, C, D, and E in Fig. 2(a), where A is the reference PV structure. These correspond to points in Fig. 5(b) defined by  $(l_b/l_c)^2 = -4.15, -4.2, -4.33, -4.5, -4.6$ , for networks A–E, respectively. The group  $l_c^2/A$  on the vertical axis of Fig. 5(b) can be computed from these values considering that  $l_c^2/A = (1/4\pi)(l_c/l_b)^2$ .

Figure 6(a) shows Cauchy stress—stretch curves for networks A to E, with increasing q values. The curves represent the mean stress over three realizations. In order to eliminate the effect of the decrease of the small strain modulus with increasing q (Fig. 5(a)), the vertical axis is normalized with  $E_0$ . All stress—stretch curves exhibit the regimes discussed in Sec. 1, and qualitatively, the NCV networks exhibit the same hyperelastic behavior as PV networks. However, significant quantitative differences are observed. As q increases, networks become softer and the range of the linear elastic regime I increases substantially. Specifically, while the PV network enters the nonlinear regime II at a strain below 5%, the NCV network with q = 4.68 enters regime II at a strain larger than 30% (Fig. 6(a)).

To emphasize this result, we compare in Fig. 7 the stress–stretch curve of network D from Fig. 6(a) with two PV networks: D1, which has the same mean segment length  $l_c$  as network D, but different density  $\rho$ , and D2, which has the same  $\rho$ , but different  $l_c$ . The two PV networks D1 and D2 do not exhibit the large increase in the range of the linear regime I observed in the NCV networks. Hence, this effect is due to the different network architecture and not to the fact that D has different  $l_c$  and/or  $\rho$ . This appears to be an intrinsic property of the NCV network architecture.

The bars in Figs. 6(a) and 7 represent the standard deviation of the three replicas used. The low replica to replica variability observed here is due to the fact that samples are large enough to render the mechanical parameters of the network model size independent [8].

Figure 6(b) shows the data in Fig. 6(a) replotted as tangent stiffness versus stress. The tangent stiffness is computed as  $E_t = \partial \sigma / \partial (\ln \lambda)$ , where  $\sigma$  is the Cauchy stress and  $\ln \lambda$  is the logarithmic strain. The left side of these curves corresponds to regime I and the value of the respective plateau is  $E_0$ . At larger stress, all curves collapse on a line of slope 1 which indicates exponential stiffening. It results that the nature of strain stiffening is independent of q. We recall that all cellular networks strain stiffen exponentially, while power law stiffening is observed in fibrous networks [17]. Very dense networks with large  $\rho_b$ , such as paper, are not hyperelastic and exhibit softening due to damage accumulation during regime I [19,60].

Figure 6(c) compares the Poisson effect in PV and NCV networks. Networks without embedding matrix generally exhibit large Poisson effect that is due to the preferential orientation of fibers in the stretch direction during regime II [61]. The large free volume of the network allows large lateral contraction upon uniaxial stretching. The figure

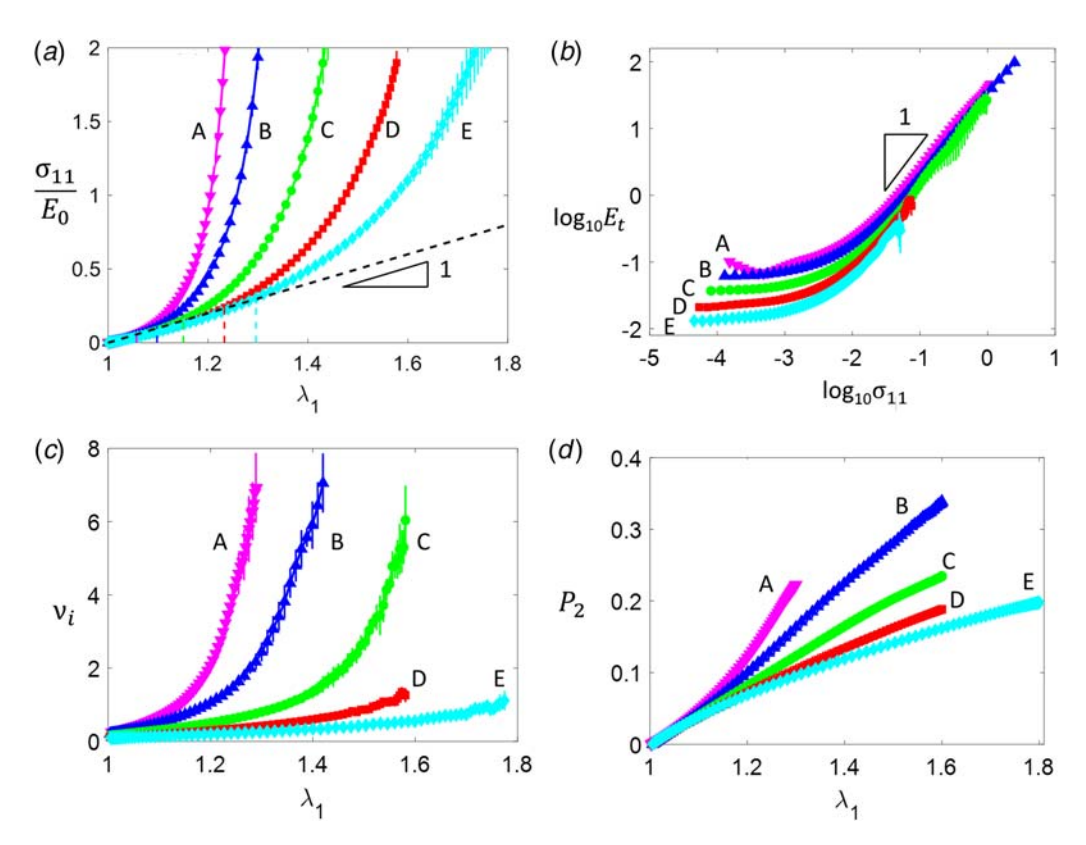


Fig. 6 (a) Cauchy stress–stretch curves for PV network A (q = 0.95) and NCV networks B, C, D, and E, with q = 1.20, 1.83, 2.94, and 4.68, respectively. The Cauchy stress is normalized with the small strain modulus  $E_0$ . The end of the linear elastic regime I for each network is indicated by a vertical dashed line. (b) Variation of the tangent stiffness modulus with the Cauchy stress. All NCV networks show the characteristic exponential stiffening in regime II. (c) Incremental Poisson ratio for the five networks indicates a reduction in Poisson contraction with an increase of q. (d) Fiber orientation index for the five networks shows less pronounced fiber reorientation during deformation in networks with larger q.

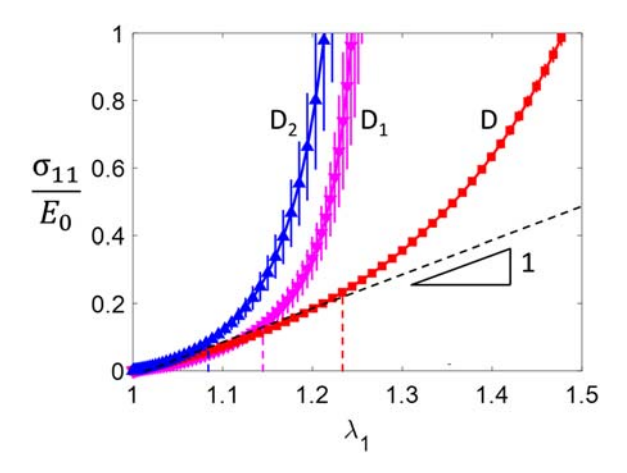


Fig. 7 Cauchy stress–stretch curves for the NCV network D and two PV networks having the same mean segment length  $I_{\rm c}$  (network D1) and same density  $\rho$  (network D2) as network D. The NCV networks have a longer-ranged linear response (regime I) than PV networks.

shows the incremental Poisson ratio defined as  $\nu_i = \partial \ln \lambda_1 / \partial \ln \lambda_2$  (where  $\ln \lambda_1$  and  $\ln \lambda_2$  are logarithmic strains in the loading and transverse directions, respectively) versus stretch. The incremental Poisson ratio reduces to the usual Poisson ratio at small strains and represents the incremental contraction rate at larger strains. In the PV case (network A),  $\nu_i$  is smaller than 0.5 at small strains and increases rapidly during regime II, with values larger than 6 being reached. NCV networks (B–E) exhibit a very different behavior. The Poisson contraction at the given stretch is much smaller than in the PV case and decreases monotonically with increasing q. The network with the largest q value does not exhibit a significant variation of the Poisson ratio during deformation.

This effect is expected considering the nonconvex nature of some of the network cells. It is known that auxetic behavior results when cell shapes are made nonconvex in solid cellular materials [62-64]. The effect observed here is of similar nature, although the structure is stochastic and not all cells are nonconvex. It is expected that the Poisson ratio can be rendered zero in NCV networks at larger (but probably physically irrelevant) q values.

The large reduction of the Poisson effect in NCV networks is of importance in applications. Most networks function while embedded in a solid or a viscoelastic or viscoplastic matrix. In gels, the deformation is isochoric if the gel is nondraining. In biological applications, drainage is slow, and tissue (e.g., ligaments, cartilage) deformation is approximately isochoric. In all these cases, the embedding medium enforces the constant volume constraint. If the embedded network has a natural tendency to contract significantly when loaded in tension, large loads are applied by the matrix on the network (and vice-versa). This leads to a more affine deformation, a stiffer effective response and likely to enhanced damage accumulation. Networks that preserve volume when not embedded, such as the NCV networks discussed here, are less incompatible with a volume preserving matrix and should develop smaller interaction forces which, in turn, should delay damage accumulation.

Figure 6(d) shows the degree of orientation of fibers during deformation for the networks considered in Fig. 6(a). The orientation is quantified with  $P_2 = \frac{1}{2}(3\cos^2\theta - 1)$ , where  $\theta$  is the angle between individual fiber orientation and the loading direction, and the overbar indicates the average over all fibers in the model. The degree of fiber orientation is smaller in NCV networks and decreases as q increases. In the PV case (network A),  $P_2$  increases rapidly once deformation enters regime II. NCV networks do not exhibit such rapid increase even after the onset of regime II.

To summarize, NCV networks are softer than the PV reference networks and exhibit two noteworthy features not commonly observed in random networks: (i) an exceptionally long-ranged linear regime I, coupled with (ii) an unusually weak Poisson effect over a broad range of strains. Both the range of the linear regime and the incremental Poisson ratio can be adjusted by controlling the degree of cell nonconvexity quantified by the parameter q.

### 5 The Strength of Nonconvex Voronoi Networks

To evaluate the strength of NCV networks, the cross-links are allowed to rupture as defined by Eq. (3). The parameter controlling the cross-link strength  $f_c$  is adjusted such that the peak stress in uni-axial tension is reached in regime II. Figure 8 shows the tensile stress–stretch curves of networks A–E. The cross-link strength  $f_c$  is identical in all these models:  $(f_c l(E_f d^2) = 2.18 \times 10^{-4})$ . Interestingly, the strength increases continuously with increasing q. The bars represent the standard deviation of three replicas. The strength increase is outside of the variability introduced by the stochastic replica microstructures. Since networks become softer as q increases, the strain corresponding to the peak stress also increases rapidly in the presence of more pronounced structural perturbation (larger  $\delta$  and q).

The strength of PV and fibrous networks was studied in detail in Ref. [31] and a relationship between strength,  $\sigma_c$ , and network parameters of type (a) and (b) was established. It was concluded that

$$\sigma_c \sim f_c \rho_b l_c \tag{4}$$

while  $\sigma_c$  is independent of fiber properties. This relation holds for fibrous and cellular PV networks and for a broad range of  $f_c$ ,  $\rho_b$ , and  $l_c$ , with the peak stress being reached in regime I (small  $f_c$ ), or at large stress and stretch values, deep into regime II (large  $f_c$ ). Networks A–E have the same  $\rho_b$  and  $f_c$  but different  $l_c$ . To test the hypothesis that the strength increase observed here is due to the increase of  $l_c$  with q, we plot in Fig. 9 the peak stress value  $\sigma_c$  versus q. The figure includes the five data points corresponding to systems A–E in Fig. 8, and additional data for NCV networks with two other  $f_c$  ( $f_c l(E_f d^2) = 1.7 \times 10^{-3}$  and  $2.18 \times 10^{-2}$ ) and  $\rho_b$  values ( $\rho_b d^3 = 8.32 \times 10^{-6}$  and  $2.35 \times 10^{-5}$ ).

Figure 9 supports the conclusion that the strengthening effect observed here is due to the increase of the mean segment length, while the cross-link density is kept constant. Given the geometric relation  $\rho = \rho_b l_c \bar{z}/2$ ,  $\rho$  increases linearly with  $l_c$  at given  $\rho_b$  and  $\bar{z}$ . Hence, the relation observed here can be also interpreted as a linear increase of  $\sigma_c$  with  $\rho$ . Such relation is usually reported in the experimental literature for networks of other architectures [19,26].

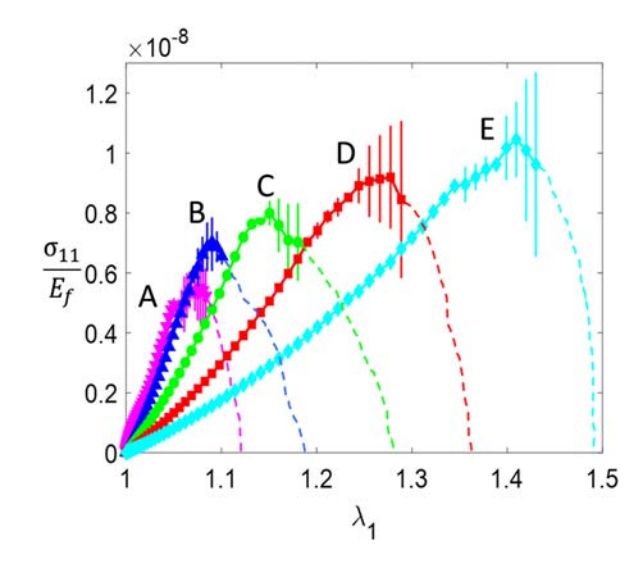


Fig. 8 Normalized Cauchy stress versus stretch curves for networks of given bond strength  $f_c/(E_td^2)=2.18\times 10^{-4}$  and bond number density  $\rho_bd^3=1.45\times 10^{-5}$  but different q. Networks A, B, C, D, and E have  $q=0.95,\ 1.20,\ 1.83,\ 2.94,\$ and  $4.68,\$ respectively.

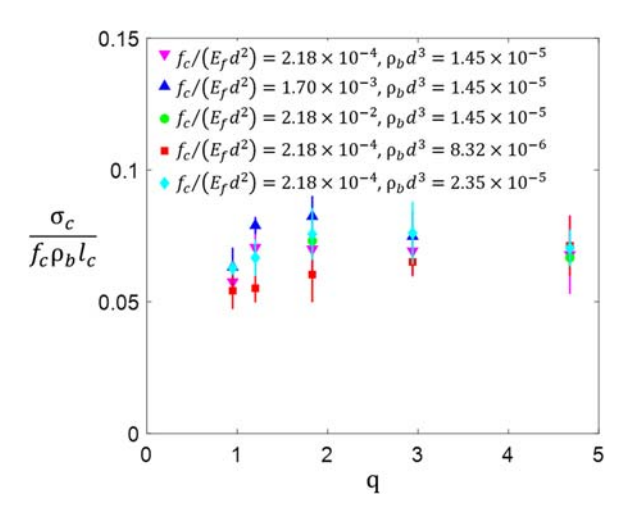


Fig. 9 Variation of the normalized strength  $\sigma_c f_c \rho_b I_c$  of NCV networks versus the degree of disorder quantified by the parameter q. Data are shown for networks of three normalized bond densities  $\rho_b d^3$  and two normalized bond strengths  $f_c / (E_f d^2)$ . The bars represent the standard deviation of three realizations.

The network strength decreases continuously with increasing model size. The proportionality constant implicit in Eq. (4) accounts for this size effect, but its variation with the model size is not analyzed in this work. This issue is discussed in detail in Ref. [25].

As mentioned above, Eq. (4) implies that the network strength is independent of the fiber elastic properties. This behavior is expected to be preserved if the fibers are rendered elastic-plastic. In this case, the constitutive response of the network would nevertheless exhibit yielding followed by plastic deformation.

These results have a two-fold importance: (a) the collapse in Fig. 9 indicates the robustness of the strength–structure relation of Eq. (4) established in Ref. [31]. It also indicates the physical origin of the increased strength of NCV networks (i.e., the increase of  $l_c$  with increasing q). (b) These results indicate ways to obtain networks that are soft, linear elastic over a large range of strains, and of high strength. This can have significant implications for network design and may lead to the development of a new class of fibrous materials.

### 6 Conclusions

A new class of cellular random networks obtained by a topological modification applied to Poisson-Voronoi networks is reported in this study. Such NCV structures have the same network parameters as the PV network, but a more disordered microstructure characterized by nonconvex cells. The degree of disorder is defined in terms of a set of structural parameters that can be measured experimentally from physical networks. Increasing the disorder increases the degree of the nonconvexity of the cells and has interesting effects on the mechanical behavior of the resulting structures. Specifically, the NCV networks are softer, but with linear elastic behavior that extends to larger strains than the reference PV network. Their Poisson contraction decreases as the degree of disorder increases. Their strength increases continuously with increasing disorder. The fact that all these properties are enhanced simultaneously renders the NCV networks of interest and suggests that unusual combinations of properties may result in regions of the design phase space that are not yet explored.

### Acknowledgment

We thank the Center for Computational Innovation (CCI) of Rensselaer Polytechnic Institute for providing access to computational resources.

### **Funding Data**

- The National Institutes of Health (NIH) (Grant No. U01 AT010326-06; Funder ID: 10.13039/100000002).
- The National Science Foundation (NSF) (Grant No. CMMI-1634328; Funder ID: 10.13039/501100008982).

## **Appendix**

Here, we present the procedure used to calculate the volume of a nonconvex cell.

Figure 10(a) shows schematically a convex cell in a PV network, prior to undergoing procedure 2 (Sec. 2). First, we calculate the position of the centroid O, of this polyhedral cell as,

$$x_i^O = \frac{\sum\limits_{n=1}^{N} x_i^n}{N} \tag{A1}$$

where N is the total number of nodes forming the cell,  $x_i^n$  is the position of the nth node in the ith direction, and  $x_i^O$  is the position of the centroid O in the ith direction.

The surface of the convex polyhedral cell is triangulated into T the number of triangles, and the cell is divided into tetrahedrons formed by each of these triangles and the centroid O (one of these, OABC is shown in the figure). The volume of the cell can be computed as sum of the volumes of all these tetrahedrons. For each of these, we determine the correct order of vector-cross product, such that the volume of the tetrahedron calculated as  $\frac{1}{6}(\overrightarrow{AB} \times \overrightarrow{AC}).\overrightarrow{OA}$  (or  $\frac{1}{6}(\overrightarrow{AC} \times \overrightarrow{AB}).\overrightarrow{OA}$ ) is positive, and the nodes are stored in the corresponding order as A–B–C (or as A–C–B).

After applying procedure 2 (Sec. 2) to obtain the nonconvex cell of Fig. 10(b), for each tetrahedron defined previously, we calculate the volume as  $\frac{1}{6}(\overrightarrow{AB} \times \overrightarrow{AC}).\overrightarrow{OA}$  (or  $\frac{1}{6}(\overrightarrow{AC} \times \overrightarrow{AB}).\overrightarrow{OA}$ ), maintaining the

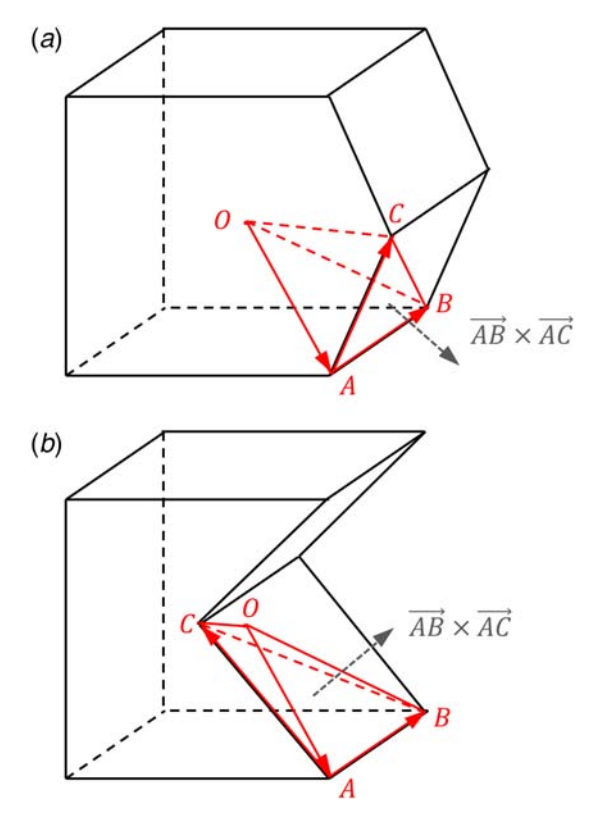


Fig. 10 (a) Schematic of a convex polyhedral cell in a PV network and (b) an example of a nonconvex mapping of the cell in (a) resulting upon the application of procedure 2

081010-8 / Vol. 86, AUGUST 2019

Transactions of the ASME

order of the nodes that were stored in the previous step and maintaining O unchanged. The volumes of some of these tetrahedrons may be negative since the dot product of a vector OA and the outward normal of the surface (defined in the previous configuration as  $\overline{AB} \times \overline{AC}$  or  $A\acute{C} \times A\acute{B}$ ) may no longer be positive. The algebraic sum of the volumes of all these tetrahedrons (with their respective signs) gives the volume of the nonconvex polyhedral cell.

#### References

- [1] Fröhlich, J., Niedermeier, W., and Luginsland, H. D., 2005, "The Effect of Filler-Filler and Filler-Elastomer Interaction on Rubber Reinforcement," Compos. Part A Appl. Sci. Manuf., 36(4), pp. 449–460.
- [2] Osada, Y., and Gong, J.-P., 1998, "Soft and Wet Materials: Polymer Gels," Adv. Mater., 10(11), pp. 827–837.
- [3] Russell, S. J., 2006, Handbook of Nonwovens, Woodhead Publishing, Cambridge.
- [4] Kannus, P., 2000, "Structure of the Tendon Connective Tissue," Scand. J. Med. ci. Sport, 10(6), pp. 312–320.
- [5] Weisel, J. W., and Litvinov, R. I., 2013, "Mechanisms of Fibrin Polymerization and Clinical Implications," Blood, 121(10), pp. 1712-1719.
- [6] Omelyanenko, N. P., and Slutsky, L. I., 2016, Connective Tissue: Histophysiology, Biochemistry, Molecular Biology, CRC Press, Boca Raton.
- [7] Head, D. A., Levine, A. J., and MacKintosh, F. C., 2003, "Distinct Regimes of Elastic Response and Deformation Modes of Cross-Linked Cytoskeletal and Semiflexible Polymer Networks," Phys. Rev. E-Stat. Physics, Plasmas, Fluids, Relat. Interdiscip. Top, **68**(6), pp. 1–15. [8] Shahsavari, A. S., and Picu, R. C., 2013, "Size Effect on Mechanical
- Behavior of Random Fiber Networks," Int. J. Solids Struct., 50(20-21), pp. 3332-3338.
- [9] Ban, E., Barocas, V. H., Shephard, M. S., and Picu, R. C., 2016, "Effect of Fiber Crimp on the Elasticity of Random Fiber Networks With and Without Embedding Matrices," ASME J. Appl. Mech., 83(4), p. 041008.
- [10] Deogekar, S., and Picu, R. C., 2017, "Structure-Properties Relation for Random Networks of Fibers With Noncircular Cross Section," Phys. Rev. E-Stat. Nonlinear, Soft Matter Phys., 95(3), p. 033001
- [11] Wilhelm, J., and Frey, E., 2003, "Elasticity of Stiff Polymer Networks," Phys. Rev. Lett., 91(10), pp. 1-4.
- [12] Huisman, E. M., Van Dillen, T., Onck, P. R., and Van Der Giessen, E., 2007, "Three-Dimensional Cross-Linked F-Actin Networks: Relation Between Network Architecture and Mechanical Behavior," Phys. Rev. Lett., 99(20), pp. 2-5.
- [13] Heussinger, C., Schaefer, B., and Frey, E., 2007, "Nonaffine Rubber Elasticity for Stiff Polymer Networks," Phys. Rev. E-Stat. Nonlinear, Soft Matter Phys., 76(3), pp. 1-12.
- [14] Onck, P. R., Koeman, T., Van Dillen, T., and Van Der Giessen, E., 2005, "Alternative Explanation of Stiffening in Cross-Linked Semiflexible Networks," Phys. Rev. Lett., **95**(17), pp. 19–22.
- [15] Broedersz, C. P., and Mackintosh, F. C., 2014, "Modeling Semiflexible Polymer Networks," Rev. Mod. Phys., 86(3), pp. 995-1036.
- [16] Licup, A. J., Münster, S., Sharma, A., Sheinman, M., Jawerth, L. M., Fabry, B., Weitz, D. A., and MacKintosh, F. C., 2015, "Stress Controls the Mechanics of Collagen Networks," Proc. Natl. Acad. Sci., 112(31), pp. 9573-9758.
- [17] Islam, M. R., and Picu, R. C., 2018, "Effect of Network Architecture on the Mechanical Behavior of Random Fiber Networks," ASME J. Appl. Mech., 85(8), p. 081011.
- [18] Magnusson, M. S., Zhang, X., and Östlund, S., 2013, "Experimental Evaluation of the Interfibre Joint Strength of Papermaking Fibres in Terms of Manufacturing Parameters and in Two Different Loading Directions," Exp. Mech., 53(9), pp. 1621-1634.
- [19] Borodulina, S., Motamedian, H. R., and Kulachenko, A., 2018, "Effect of Fiber and Bond Strength Variations on the Tensile Stiffness and Strength of Fiber Networks," Int. J. Solids Struct., **154**, pp. 19–32. [20] Borodulina, S., Kulachenko, A., Nygards, M., and Galland, S., 2012,
- "Stress-Strain Curve of Paper Revisited," Nord. Pulp Pap. Res. J., 27(2), pp. 318-328.
- [21] Chen, N., and Silberstein, M. N., 2018, "Determination of Bond Strengths in Non-Woven Fabrics: A Combined Experimental and Computational Approach," Exp. Mech., **58**(2), pp. 343–355.
- [22] Chen, N., Koker, M. K. A., Uzun, S., and Silberstein, M. N., 2016, "In-Situ X-Ray Study of the Deformation Mechanisms of Non-Woven Polypropylene," Int. J. Solids Struct., **97–98**, pp. 200–208.
- [23] Farukh, F., Demirci, E., Sabuncuoglu, B., Acar, M., Pourdeyhimi, B., and Silberschmidt, V. V., 2014, "Numerical Analysis of Progressive Damage in Nonwoven Fibrous Networks Under Tension," Int. J. Solids Struct., 51(9), pp. 1670-1685.
- [24] Ridruejo, A., González, C., and Llorca, J., 2011, "Micromechanisms of Deformation and Fracture of Polypropylene Nonwoven Fabrics," Int. J. Solids Struct., **48**(1), pp. 153–162.
- [25] Deogekar, S., and Picu, R. C., 2018, "On the Strength of Random Fiber Networks," J. Mech. Phys. Solids, 116, pp. 1–16.
- [26] Heyden, S., and Gustafsson, P. J., 1998, "Simulation of Fracture in a Cellulose Fibre Network," J. Pulp Pap. Sci., 25(5), pp. 160-165.

- [27] Hadi, M. F., and Barocas, V. H., 2013, "Microscale Fiber Network Alignment Affects Macroscale Failure Behavior in Simulated Collagen Tissue Analogs, J. Biomech. Eng., 135(2), p. 021026.
- [28] Berhan, L., and Sastry, A. M., 2003, "On Modeling Bonds in Fused, Porous Networks: 3D Simulations of Fibrous-Particulate Joints," J. Compos. Mater., 37(8), pp. 715-740.
- [29] Koh, C. T., Strange, D. G. T., Tonsomboon, K., and Oyen, M. L., 2013, "Failure Mechanisms in Fibrous Scaffolds," Acta Biomater, 9(7), pp. 7326–7334.
- [30] Goutianos, S., Mao, R., and Peijs, T., 2018, "Effect of Inter-Fibre Bonding on the Fracture of Fibrous Networks with Strong Interactions," Int. J. Solids Struct., 136, pp. 271-278.
- [31] Deogekar, S., Islam, M. R., and Picu, R. C., 2019, "Parameters Controlling the Strength of Stochastic Fibrous Materials," Int. J. Solids Struct., 168, pp. 194-202.
- [32] Shahsavari, A. S., and Picu, R. C., 2013, "Elasticity of Sparsely Cross-Linked Random Fibre Networks," Philos. Mag. Lett., 93(6), pp. 356–361.
  [33] Gibson, L. J., and Ashby, M. F., 1999, Cellular Solids: Structure and Properties,
- Cambridge University Press, Cambridge. [34] Lederman, J. M., 1971, "The Prediction of the Tensile Properties of Flexible
- Foams," J. Appl. Polym. Sci., 15(3), pp. 693-703.
- [35] Gent, A. N., and Thomas, A. G., 1959, "The Deformation of Foamed Elastic Materials," J. Appl. Polym. Sci., 1(1), pp. 107-113.
- [36] Vader, D., Kabla, A., Weitz, D., and Mahadevan, L., 2009, "Strain-Induced Alignment in Collagen Gels," PLoS One, 4(6), p. e5902.
- Verhille, G., Moulinet, S., Vandenberghe, N., Adda-Bedia, M., and Le Gal, P., 2017, "Structure and Mechanics of Aegagropilae Fiber Network," Proc. Natl. Acad. Sci., 114(18), pp. 4607-4612.
- [38] Grenestedt, J. L., and Tanaka, K., 1998, "Influence of Cell Shape Variations on Elastic Stiffness of Closed Cellular Solids," Scr. Mater., 40(1), pp. 71-77.
- [39] Roberts, A. P., and Garboczi, E. J., 2002, "Elastic Properties of Model Random Three-Dimensional Open-Cell Solids," J. Mech. Phys. Solids, 50(1), pp. 33–55.
- [40] Zhou, J., Mercer, C., and Soboyejo, W. O., 2002, "An Investigation of the Microstructure and Strength of Open-Cell 6101 Aluminum Foams," Metall. Mater. Trans. A, 33(5), pp. 1413-1427.
- [41] Sotomayor, O. E., and Tippur, H. V., 2014, "Role of Cell Regularity and Relative Density on Elastoplastic Compression Response of 3-D Open-Cell Foam Core Sandwich Structure Generated Using Voronoi Diagrams," Acta Mater., 78, pp. 301-313.
- [42] Luxner, M. H., Stampfl, J., and Pettermann, H. E., 2007, "Numerical Simulations of 3D Open Cell Structures-Influence of Structural Irregularities on Elasto-Plasticity and Deformation Localization," Int. J. Solids Struct., 44(9), pp. 2990-3003.
- [43] Li, K., Gao, X.-L., and Subhash, G., 2006, "Effects of Cell Shape and Strut Cross-Sectional Area Variations on the Elastic Properties of Three-Dimensional Open-Cell Foams," J. Mech. Phys. Solids, 54(4), pp. 783-806.
- [44] Picu, R. C., Sorohan, S., Soare, M. A., and Constantinescu, D. M., 2016, "Towards Designing Composites With Stochastic Composition: Effect of Fluctuations in Local Material Properties," Mech. Mater., 97, pp. 59–66.
- [45] Huyse, L., and Maes, M. A., 2001, "Random Field Modeling of Elastic Properties
- Using Homogenization," J. Eng. Mech., 127(1), pp. 27–36. [46] Negi, V., and Picu, R. C., 2018, "Elastic-Plastic Transition in Stochastic Heterogeneous Materials: Size Effect and Triaxiality," Mech. Mater., 120, pp. 26-33.
- [47] Lucarini, V., 2009, "Three-Dimensional Random Voronoi Tessellations: From Cubic Crystal Lattices to Poisson Point Processes," J. Stat. Phys., 134(1),
- [48] Kallmes, O., and Corte, H., 1960, "The Structure of Paper-The Statistical Geometry of an Ideal Two Dimensional Fiber Network," Tappi J., 43(9), pp. 737-752.
- [49] Kantaros, A., Chatzidai, N., and Karalekas, D., 2016, "3D Printing-Assisted Design of Scaffold Structures," Int. J. Adv. Manuf. Technol., 82(1-4), pp. 559-
- [50] Warnke, P. H., Seitz, H., and Warnke, F., 2010, "Ceramic Scaffolds Produced by Computer-Assisted 3D Printing and Sintering: Characterization and Biocompatibility Investigations," J. Biomed. Mater. Res. Part B Appl. Biomater, 93(1), pp. 212–217.
- [51] Singh, S., and Ramakrishna, S., 2017, "Biomedical Applications of Additive Manufacturing: Present and Future," Curr. Opin. Biomed. Eng., 2, pp. 105-115.
- [52] Vail, N. K., Swain, L. D., and Fox, W. C., 1999, "Materials for Biomedical Applications," Mater. Des., 61(1-2), pp. 168-172.
- [53] Tan, K. H., Chua, C. K., and Leong, K. F., 2003, "Scaffold Development Using Selective Laser Sintering of Polyetheretherketone-Hydroxyapatite Biocomposite Blends," Biomaterials, **24**(18), pp. 3115–3123.
- Yan, C., Hao, L., and Hussein, A., 2015, "Ti-6Al-4 V Triply Periodic Minimal Surface Structures for Bone Implants Fabricated via Selective Laser Melting," J. Mech. Behav. Biomed. Mater., 51, pp. 61-73.
- [55] Parthasarathy, J., Starly, B., and Raman, S., 2010, "Mechanical Evaluation of Porous Titanium (Ti6Al4 V) Structures with Electron Beam Melting (EBM),"
- J. Mech. Behav. Biomed. Mater., 3(3), pp. 249–259. [56] Martínez, J., Dumas, J., and Lefebvre, S., 2016, "Procedural Voronoi Foams for Additive Manufacturing," ACM Trans. Graph., 35(4), p. 44.
- [57] Magnusson, M. S., 2014, Interfibre Joint Strength Under Mixed Modes of Loading, KTH Royal Institute of Technology, Stockholm, Sweden.
- [58] Kasza, K. E., Broedersz, C. P., Koenderink, G. H., Lin, Y. C., Messner, W., Millman, E. A., Nakamura, F., Stossel, T. P., Mackintosh, F. C., and Weitz, D. A., 2010, "Actin Filament Length Tunes Elasticity of Flexibly Cross-Linked Actin Networks," Biophys. J., 99(4), pp. 1091-1100.

- [59] Fallqvist, B., Kulachenko, A., and Kroon, M., 2014, "Modelling of Cross-Linked Actin Networks—Influence of Geometrical Parameters and Cross-Link Compliance," J. Theor. Biol., 350, pp. 57–69.
- [60] Kulachenko, A., and Uesaka, T., 2012, "Direct Simulations of Fiber Network Deformation and Failure," Mech. Mater., 51, pp. 1–14.
  [61] Picu, R. C., Deogekar, S., and Islam, M. R., 2018, "Poisson's Contraction and
- [61] Picu, R. C., Deogekar, S., and Islam, M. R., 2018, "Poisson's Contraction and Fiber Kinematics in Tissue: Insight From Collagen Network Simulations," ASME J. Biomech. Eng., 140(2), p. 021002.
- [62] Evans, K. E., Alderson, A., and Christian, F. R., 1995, "Auxetic Two-Dimensional Polymer Networks. An Example of Tailoring Geometry for Specific Mechanical Properties," J. Chem. Soc. Faraday Trans., 91(16), pp. 2671–2680.
- [63] Prawoto, Y., 2012, "Seeing Auxetic Materials From the Mechanics Point of View: A Structural Review on the Negative Poisson's Ratio," Comput. Mater. Sci., 58, pp. 140–153.
- [64] Alderson, A., and Alderson, K. L., 2007, "Auxetic Materials," Proc. Inst. Mech. Eng. Part G J. Aerosp. Eng., 221(4), pp. 565–575.